0.1 E06-014

Precision Measurement of d_2^n: Probing the Lorentz Color Force

S. Choi, X. Jiang, Z.-E. Meziani, B. Sawatzky, spokespersons,
and
the d_2^n and Hall A Collaborations.
contributed by M. Posik, L. El Fassi, D. Flay, D. Parno, and Y. Zhang.

0.1.1 The Experiment

Experiment E06-014 ran in Hall A from February 7 to March 17, 2009, at two production beam energies of 4.73 and 5.89 GeV, on a polarized ^{3}He target. The experiment probed the resonance and deep inelastic valence quark regions, which corresponded to the ranges $0.15 \leq x \leq 1.0$ and 1.5 GeV$^2 \leq Q^2 \leq 7$ GeV^2. Figure 1 shows the coverage in Q^2 and x. Included in this plot is the invariant mass W at a value of 2 GeV, which separates the resonance and deep inelastic regions. The LHRS and BigBite detector packages were each oriented at 45° relative to the beam line, with each of the detectors independent of one another, acting as its own single-arm experiment. The LHRS was used to measure the unpolarized cross-section, while the BigBite measured the double-spin asymmetries in scattering between a longitudinally polarized electron beam and a longitudinally and transversely polarized ^{3}He target.

E06-014 also served as the commissioning experiment for a gas Čerenkov detector, which was installed into the the BigBite stack, as well as a new photon detector and integrating data-acquisition system for the Compton polarimeter [1, 2, 3, 4].

The primary goal of E06-014 is the measurement of the quantity d_2^n. The neutron d_2 is a probe of the strong force that is formed by taking the second moment of a linear combination of the polarized structure functions g_1 and g_2:

$$d_2^n\left(Q^2\right) = \int_0^1 x^2 \left[2g_1^n\left(x, Q^2\right) + 3g_2^n\left(x, Q^2\right)\right] dx. \tag{1}$$

At low Q^2 where the virtual photon wavelength is larger than the nucleon, d_2 can be associated with spin polarizabilities within the nucleon [5, 6]. However, at larger Q^2, it is more appropriate to interpret d_2 as the average transverse Lorentz color force acting on a quark after being hit by a virtual photon [5, 7].

In addition to gaining insight into the nature of the color force, the precision measurement of d_2^n will also be a benchmark test for lattice QCD predictions.

E06-014 measured d_2^n by combining the unpolarized cross-section, σ_0 from the LHRS, as well as the parallel and perpendicular asymmetries, $A_\parallel$ and $A_\perp$ from BigBite. The asymmetries are defined through the counting rates of each spin orientation as:

$$A_\parallel = \frac{N^{\downarrow\Uparrow} - N^{\uparrow\Uparrow}}{N^{\downarrow\Uparrow} + N^{\uparrow\Uparrow}} \quad \text{and} \quad A_\perp = \frac{N^{\downarrow\Rightarrow} - N^{\uparrow\Rightarrow}}{N^{\downarrow\Rightarrow} + N^{\uparrow\Rightarrow}},$$

where single arrows represent the electron helicity direction, and double arrows represent the target polarization direction. By combining these independently measured quantities, d_2^n is expressed exclusively through experimental quantities as:

$$d_2^n = \int_0^1 \frac{MQ^2}{4\alpha^2} \frac{x^2 y^2}{(1-y)(2-y)} \sigma_0 \left[\left(3\frac{1 + (1-y)\cos\theta}{(1-y)\sin\theta} + \frac{4}{y}\tan\left(\theta/2\right)\right) A_\perp + \left(\frac{4}{y} - 3\right) A_\parallel\right] dx, \tag{2}$$

where $\nu = E - E'$ is the energy transfer from electron to target, θ is the scattering angle of the electron and $y = \nu/E$ is the fractional energy transfer from electron to target. The advantage of measuring d_2^n in terms of experimental quantities is that it allowed the allotted beam time to be divided between measuring $A_\parallel$ and $A_\perp$ in such a way that the error on d_2^n was minimized, rather than minimizing the error on the spin structure functions g_1^n and g_2^n. The measurement of $d_2^n\left(Q^2 \approx 3 \text{ GeV}^2\right)$ is expected to result in a fourfold improvement on the world data as shown in Figure 2, in advance of an approved 12 GeV experiment in Hall C that will extend the precision measurement of d_2^n to higher kinematic ranges [16].
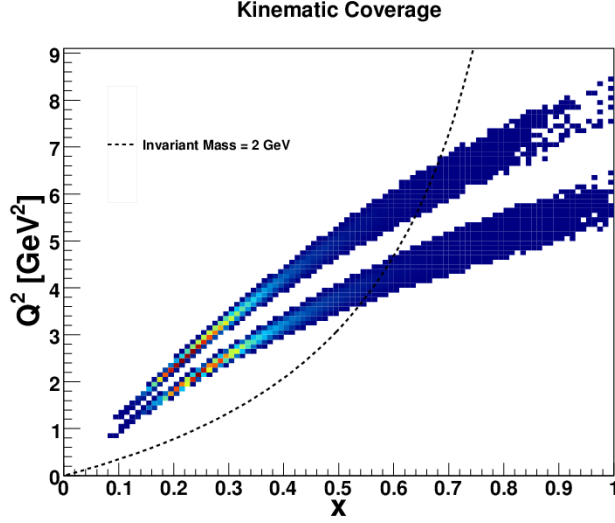
Figure 1: Shown is E06-014's coverage in Q^2 and x. The lower band is the 4.73 GeV dataset and the upper band is the 5.89 GeV dataset. The black dashed line shows $W = 2$ GeV. $W < 2$ GeV corresponds to x values to the right of the dashed line, which distinguishes the resonance region. $W > 2$ GeV corresponds to the x values to the left of the dashed line, which defines the deep inelastic region.

In addition to the primary goal of E06-014, the data collected can also be used to measure the longitudinal virtual photon-nucleon asymmetry for the neutron, A_1^n. The virtual photon-nucleon scattering cross section can be separated into two helicity-dependent cross sections, $\sigma_{1/2}$ and $\sigma_{3/2}$. The subscript $1/2(3/2)$ gives the projection of the total spin along the virtual photon's momentum direction, corresponding to anti-parallel (parallel). A_1 can then be defined as:

$$A_1\left(x, Q^2\right) \equiv \frac{\sigma_{1/2} - \sigma_{3/2}}{\sigma_{1/2} + \sigma_{3/2}} \approx \frac{g_1\left(x, Q^2\right)}{F_1\left(x, Q^2\right)} \text{ for high } Q^2, \tag{3}$$

were F_1 is the unpolarized structure function. We may also express A_1 in terms of the parallel and perpendicular asymmetries, $A_\parallel$ and $A_\perp$, that were measured in BigBite as:

$$A_1 = \frac{1}{D\left(1 + \eta\xi\right)} A_\parallel - \frac{\eta}{d\left(1 + \eta\xi\right)} A_\perp \tag{4}$$

where D is the virtual photon polarization factor and η, ξ, and d are quantities set by kinematics and by the virtual photon polarization vector [2].

Combining A_1^n data measured on an polarized effective neutron target with A_1^p data measured on a polarized proton target, allows access to the polarized-unpolarized parton distribution function ratios $\Delta u/u$ and $\Delta d/d$. Recent results from Hall A [17] and from CLAS [18] showed a significant deviation of $\Delta d/d$ from the predictions of perturbative QCD, which have that ratio approaching 1 in the limit of $x \to 1$. As part of the 12 GeV program, two approved experiments (one in Hall A [19] and one in Hall C [20]) will extend the accuracy and x range of this measurement, but a measurement of A_1^n at E06-014's kinematics will provide valuable support (or refutation) of prior Jefferson Lab results, while producing additional input for theoretical models in advance of the coming experiments at 12 GeV.

0.1.2 Analysis Progress: Target and Beam

When performing a double-spin asymmetry experiment, knowledge of the target and beam polarization is crucial. E06-014 used the standard Hall A polarized ^{3}He target with two holding field directions: longitudinal and transverse in plane with respect to the beam direction. To extract the target polarization, EPR and NMR measurements were done. Since the calculation of target polarization from EPR and NMR measurements depends on the ^{3}He density, a complete understanding of the density is essential.
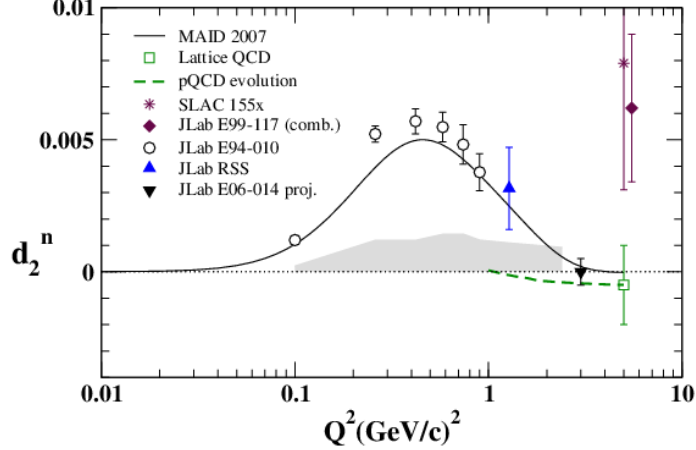
Figure 2: The projected error on from E06-014 [8] is shown, along with the lattice QCD result [9]. The pQCD evolution from the lattice point was performed by Patricia Solvignon, which was based on papers by Shuyak and Vainshein [10] and Ji and Chou [11]. Data from JLab experiments E94-010 [12] and RSS [13] are included in the plot. For comparison to the resonance contribution, a MAID model [14] is plotted. Also plotted is the total d_2 from SLAC exeriment E155x [15].

The number density of ^{3}He was measured in both the pumping chamber and the target chamber. This measurement was achieved by using the fact that collisions with ^{3}He atoms broaden the D1 and D2 absorption lines of rubidium [21]. By measuring the width of the D1 and D2 absorption lines and subtracting a 1% N_2 contribution, a measurement of n_0, the ^{3}He number density at room temperature can be obtained.

$$n_{pc} = n_0 \left[1 + \frac{V_{pc}}{V_{tot}} \left(\frac{T_{tc}}{T_{pc}} - 1 \right) \right]^{-1} \tag{5}$$

$$n_{tc} = n_0 \left[1 + \frac{V_{tc}}{V_{tot}} \left(\frac{T_{pc}}{T_{tc}} - 1 \right) \right]^{-1} \tag{6}$$

Since the number density changes with temperature, Equations 5 and 6 were used to compute the number densities[1] in both the pumping and target chambers, where V_{tot} is the total volume of the target cell, T is the temperature and the subscripts pc (tc) refer to the pumping (target) chamber. The temperature of the chambers was measured using seven resistive thermal devices (RTDs), which were placed outside of the target and were stable within 2°C during production [2]. The ^{3}He number densities for the E06-014 target cell, Samantha, as a function of run number can be seen in Figure 3, with the average values listed in Table 1.

Chamber	^{3}He Density (amg)
Pumping	6.93 ± 0.19
Target	10.81 ± 0.29

Table 1: Average ^{3}He densities in target cell [2, 22]

During E06-014, EPR measurements were taken every several days, while NMR measurements were taken every four hours. During EPR measurements, the frequency shift of potassium level transitions in the presence of polarized ^{3}He was measured. This frequency shift $\Delta\nu_{EPR}$ can be related to the target polarization, $P_{^3\text{He}}$:

$$\Delta\nu_{EPR} = \frac{4\mu_0}{3} \frac{d\nu_{EPR}}{dB} \kappa_0 \mu_{^3\text{He}} n_{pc} P_{^3\text{He}}, \tag{7}$$

---

[1]Densities were calculated in units of amagat, where an amagat (amg) is 2.687×10^{25} m^{-3}.

3

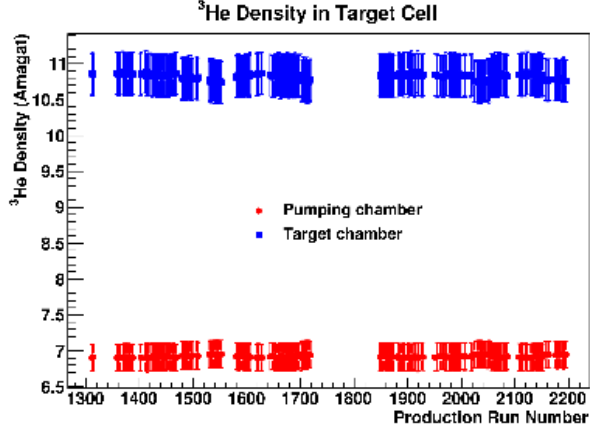Figure 3: ^{3}He densities as a function of BigBite run number [2]

where μ_0 is the vacuum permeability, $\mu_{^3\text{He}}$ is the magnetic moment, $\frac{d\nu_{EPR}}{dB}$ is the derivative of the EPR frequency with respect to the magnetic field, κ_0 is the enhancement factor and n_{pc} is the pumping chamber number density. During EPR measurements, a NMR measurement was done simultaneously. This allows for a comparison between the EPR polarization, $P_{^3\text{He}}$, and the measured NMR amplitude, h. A conversion factor c' can then be formed that allows NMR measurements to be converted into an absolute ^{3}He polarization, and is defined as:

$$c' = \frac{P_{^3\text{He}}}{h}. \tag{8}$$

In addition to obtaining the conversion factor c' from comparing EPR and NMR measurements, it can also be calculated by performing a calibration on a water target. The final NMR polarization is then computed by taking the weighted average of the polarization computed from the EPR and water calibrations. Although the water calibration still needs to be done in order to obtain the final target polarization, the EPR measurements can be used to obtain a preliminary target polarization. The average conversion factor c' for all EPR measurements in each target polarization direction, which can be seen in Table 2, was computed and applied to the NMR measurements. A linear interpolation was then done in order to obtain the polarization on a run-by-run basis. This procedure resulted in a combined systematic and statistical error of 4.9% as shown in Figure 4 [2, 22].

Polarization Direction	$c'(\%/\text{mV})$
Longitudinal	2.84 ± 0.14
Transverse	1.77 ± 0.09

Table 2: EPR-NMR conversion factors c' [2, 23]

In addition to the target polarization, the beam polarization also needs to be known. E06-014 used a polarized electron beam at energies of 4.73 and 5.89 GeV. The polarization of the electron beam was measured independently through Compton and Møller scattering. During the running of E06-014, there were several Møller measurements performed, while Compton measurements were taken continuously throughout the experiment. Figure 5 shows the beam polarization as a function of BigBite run number for the Møller and Compton results. The beam polarization data was split into four run sets and the average polarization for each run period was then computed by taking into account both the Compton and Møller data. The final beam polarizations can be seen in Table 3 [2].
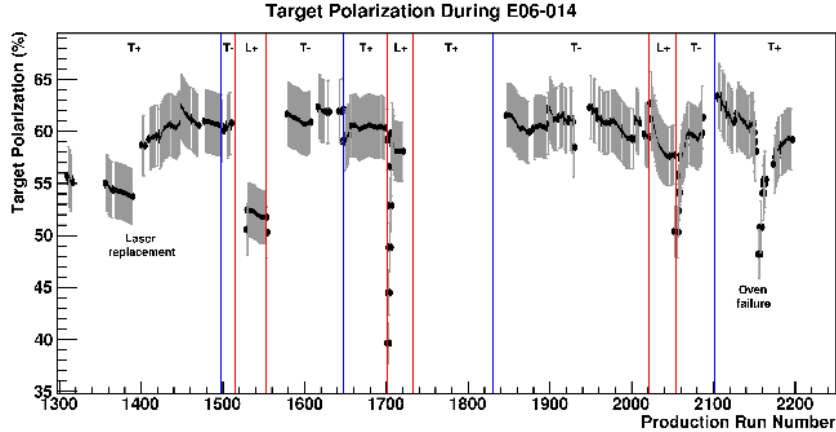
Figure 4: Preliminary target polarization based on linear interpolation of NMR polarization measurements calibrated using EPR results. Red lines show spin transitions between transverse and longitudinal orientations. Blue lines show 180° rotations of spin orientation within a polarization plane. The labels at the top of the graph give the polarization direction during that time period: $L_+ = 0°$, $T_- = 90°$ and $T_+ = 270$ [2].

Run Set	Beam Energy (GeV)	P_e from Compton	P_e from Møller	Combined P_e
1	5.90	0.726 ± 0.018	0.745 ± 0.015	0.737 ± 0.012
2	4.74	0.210 ± 0.011	-	0.210 ± 0.011
3	5.90	0.787 ± 0.020	0.797 ± 0.016	0.793 ± 0.012
4	4.74	0.623 ± 0.016	0.628 ± 0.012	0.626 ± 0.010

Table 3: Final beam polarization for E06-014, corrected for beam fluctuations. For run set 2 there was no Møller measurement. [2]

0.1.3 Analysis Progress: LHRS

The LHRS was used to measure the total unpolarized cross section, which will multiply the measured asymmetries in BigBite. In order to measure the unpolarized cross section, the LHRS hardware must be calibrated and particle identification (PID) cuts applied in order to select a particular particle type from the data [1]. The total unpolarized cross section is given as:

$$\sigma_0 = \frac{N \cdot ps \cdot e}{\epsilon \cdot w \cdot Q \cdot t_{LT} \cdot n \cdot \Delta Z \Delta\theta \Delta\phi \Delta E'},$$ (9)

where N is the number of events counted that passed the PID cuts, ps is the pre-scale factor, ϵ is the detector efficiency, Q is the the total charge on target, t_{LT} is the trigger live time, n is the target density, ΔZ is the effective target length as seen by the LHRS, $\Delta\theta$ is the vertical (dispersive) angle, $\Delta\phi$ is the horizontal (transverse) angle, $\Delta E'$ is the electron energy width seen by the LHRS, and w is an acceptance weight factor.

Due to the fields created by the LHRS magnets, the actual acceptance may not coincide with the geometrical apretures of the LHRS. To account for this difference, a weight factor is computed. In order to determine the weight factor w, a Single Arm Monte Carlo (SAMC) simulation was utilized. The simulation randomly generates particle trajectories that are larger in momentum and solid angle ranges than the actual acceptance. The same cuts that are used in determining the electron events from production data are then applied to the events generated from SAMC. This event count will now be referred to as N_{MC}^{trial}. The simulation then uses John LeRose's transport matrices [24], to propagate the N_{MC}^{trial} events through the LHRS. As the particle approaches each magnet aperture in the LHRS, a check is performed to see if the particle passes through the aperture. For all events that make it to the focal plane, the event is reconstructed at the target. These events are referred to as N_{MC}^{acc}. The ratio of $\frac{N_{MC}^{acc}}{N_{MC}^{trial}}$ then forms the acceptance weight factor w [25]. In Figure 6, we see the results from SAMC compared to actual production data for the target length
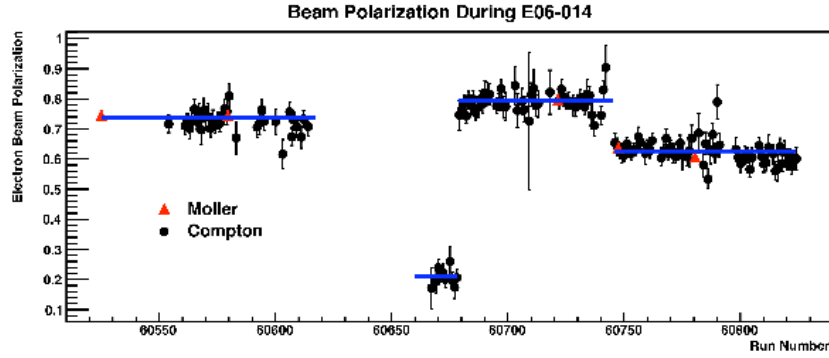
5

Figure 5: Final electron beam polarization from Møller and Compton measurements for E06-014. Note there was no Møller measurement for the second run set [2].
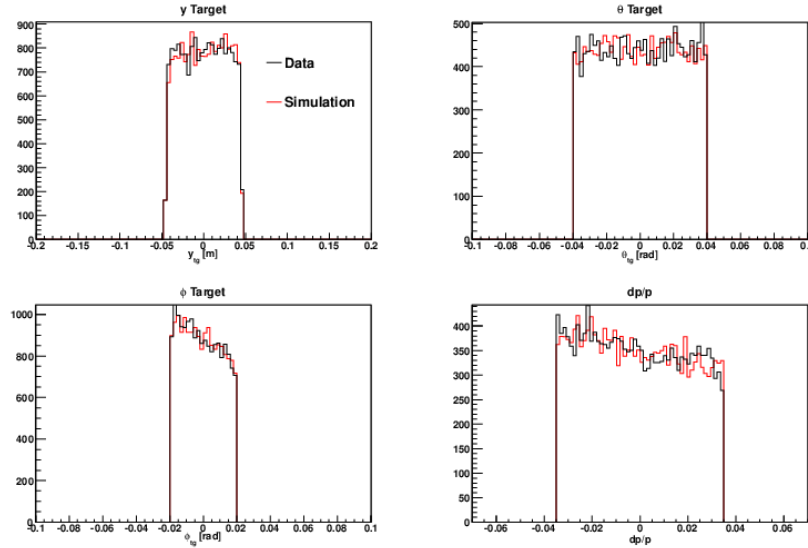

Figure 6: Comparison of events that passed in SAMC to E06-014 production data from LHRS.

seen by the LHRS, the vertical and horizontal angular distributions and $\delta p/p$. The acceptance weight is approximately 0.99.

The raw ^{3}He cross-section that was measured in the LHRS, σ_{raw}, contains contributions from electrons which do not originate from scattering off of ^{3}He nuclei, but rather from pair production processes and scattering from nitrogen nuclei. Nitrogen gas is present in the pumping chamber to optimize ^{3}He polarization [21]. Some of the nitrogen gas diffuses from the pumping chamber into the target chamber where interactions with the electron beam take place. In order to remove the pair production and nitrogen contributions from σ_{raw}, several runs were taken with the LHRS in positive polarity mode during which positrons were detected. From these runs a positron cross-section, σ_{e+}, was measured. To obtain the nitrogen scattering contribution that is present during ^{3}He runs, a reference target cell was used. The reference cell was similar in geometry to the ^{3}He cell but was filled with nitrogen gas. By scattering electrons from the nitrogen target, a nitrogen cross-section, $\sigma_{N_2}^{e-}$ was measured. Since pair production is also present when scattering electrons off of nitrogen nuclei, a nitrogen positron cross-section, $\sigma_{N_2}^{e+}$ was also measured with the LHRS in positive polarity mode. The nitrogen positron cross-section was subtracted from the nitrogen cross-section to avoid double counting pair production events which were already accounted for in the ^{3}He positron cross-section. In order to account for the probability of scattering from nitrogen nuclei present in the ^{3}He target
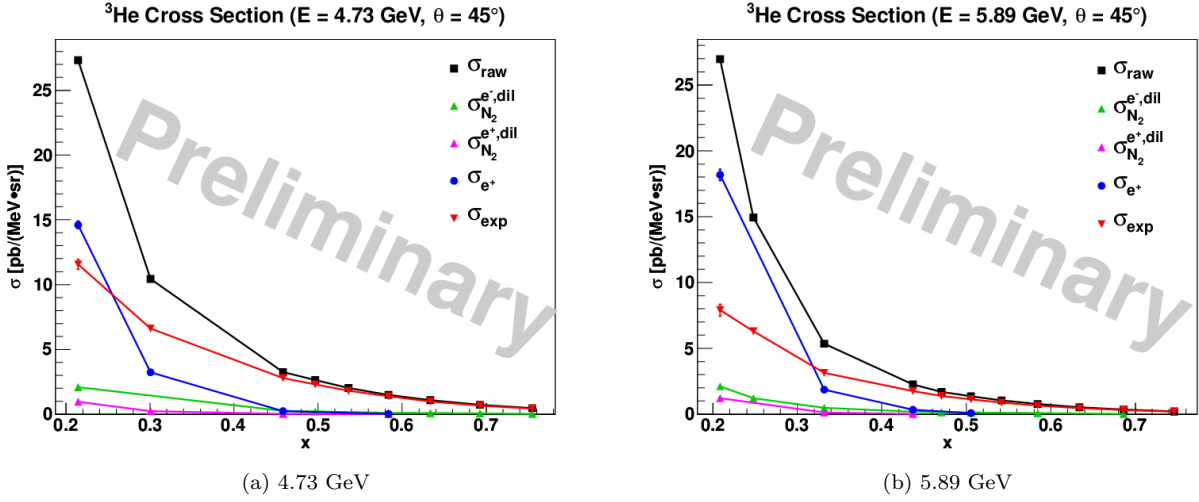
6

(a) 4.73 GeV

(b) 5.89 GeV

Figure 7: LHRS preliminary cross sections as a function of x. Radiative corrections have not been applied to the cross sections, and error bars shown are statistical only.

cell, the nitrogen cross-sections were weighted by the atomic densities. The weighted nitrogen cross-section, $\sigma_{N_2}^{dil}$, is called the diluted nitrogen cross-section and is defined as:

$$\sigma_{N_2}^{dil} = \frac{n_{N_2}}{n_{N_2} + n_{^3He}} \left(\sigma_{N_2} - \sigma_{N_2}^{e+} \right) = \sigma_{N_2}^{dil,e-} - \sigma_{N_2}^{dil,e+}, \tag{10}$$

where n_{N_2} and $n_{^3He}$ are the nitrogen and ^3He densities.

σ_{raw} can now be corrected for pair production processes and nitrogen scattering contributions by:

$$\sigma_{exp} = \sigma_{raw} - \sigma_{e+} - \sigma_{N_2}^{dil} \tag{11}$$

Figure 7 shows the 4.73 and 5.89 GeV raw, positron, nitrogen, diluted nitrogen and corrected cross-sections measured in the LHRS as a function of x. With the preliminary 4.73 and 5.89 GeV cross-sections completed, analysis is now being done on radiative corrections and fitting the cross-section data.

0.1.4   Analysis Progress: BigBite

E06-014 used the BigBite detector package to measure the double spin asymmetry between longitudinally polarized electrons and a longitudinally and transversely polarized ^3He target. The BigBite detector calibrations and data quality checks have been completed for the 4.73 GeV data set [1, 2]. Preliminary asymmetry analysis at a beam energy of 4.73 GeV has also been completed. The longitudinal and transverse asymmetries were computed using Equation 2. The kinematic range ($0.15 \leq x \leq 1.0$) has been divided into 17 equally spaced x bins. As can be seen from Figure 1, this data set is in the deep-inelastic scattering (DIS) regime ($W > 2$) for $x \leq 0.52$; above this value, the data are in the resonance region.

Since the ^3He target has a small percentage of N_2 present, as shown in Section 0.1.3, the unpolarized N_2 gas will tend to dilute the measured asymmetries. In order to correct for this in BigBite, counting rates from a pure N_2 target was also measured. Comparing the N_2 target counting rates to the ^3He production cell scattering rates, a dilution factor can be formed and applied to the measured asymmetry. The dilution factor is given by Equation (12):

$$D_{N_2} = 1 - \frac{\Sigma_{N_2}(N_2)}{\Sigma_{total}(^3He)} \frac{Q(^3He)n_{N_2}(^3He)}{Q(N_2)n_{N_2}(N_2)}, \tag{12}$$

where Σ_{N_2} and Σ_{total} are the total scattering counts that pass data-quality and PID cuts detected during the N_2 and ^3He target runs. $Q(N_2)$ and $Q(^3He)$ are the total charge deposited on the two targets and

$n_{\mathrm{N_2}}(\mathrm{N_2})$ and $n_{\mathrm{N_2}}(^3\mathrm{He})$ are the nitrogen number densities present in the two targets. The dilution factor was computed at each of the 17 x bins. Figure 8 shows the results of the nitrogen dilution calculations.
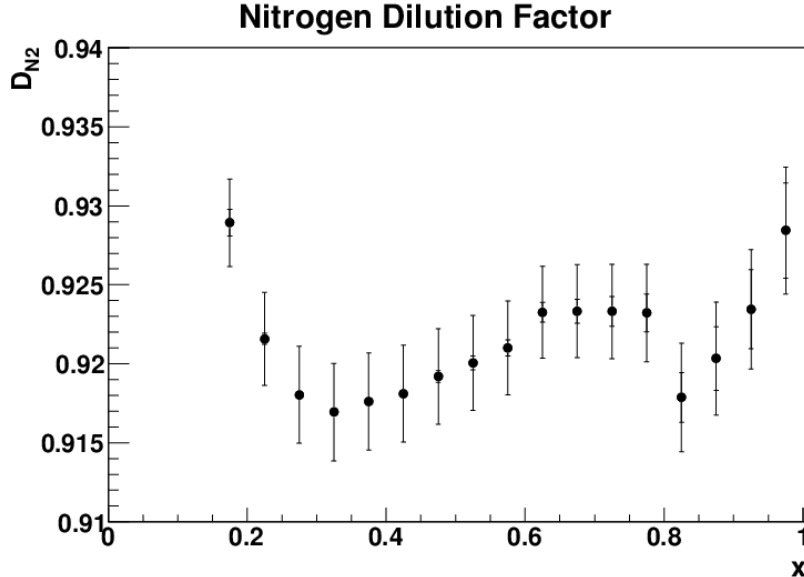

Figure 8: Preliminary $\mathrm{N_2}$ dilution factor is plotted vs x at a beam energy of 4.73 GeV. Outer error bars show combined systematic and statistical errors. The inner error bars show only statistical errors. In some bins, the statistical error is too small to be seen on the graph.

In addition to correcting for nitrogen dilution, corrections for target and beam polarizations must also be applied since the target and beam were not fully polarized. This is accounted for by dividing the asymmetries by the measured target and beam polarizations, P_t and P_b, found in Figure 4 and Table 3. The physics asymmetries are then given as:

$$A_{\parallel} = \frac{1}{P_b P_t D_{\mathrm{N_2}}} A_{\parallel}^{raw}, \ A_{\perp} = \frac{1}{P_b P_t D_{\mathrm{N_2}}\cos(\phi)} A_{\perp}^{raw}, \tag{13}$$

where ϕ is the vertical scattering angle. Figure 9 shows the physics asymmetries on ^{3}He at an electron beam energy of 4.73 GeV as a function of x. These asymmetries can also be used to form longitudinal virtual photon-nucleus asymmetry on ^{3}He, $A_1^{^3\mathrm{He}}$ via Equation 4. Preliminary E06-014 A_1 asymmetry measurements on ^{3}He are in good agreement with previous A_1 asymmetry measurements, as can be seen in Figure 10. E06-014's largest sources of systematic error on the 4.73 GeV data set are due to the target polarization measurement, the contamination of the DIS electron sample by pair-production processes, and errors in momentum assignment. Completing and finalizing the target water calibration will substantially reduce the systematic error. A complete study of backgrounds must await analysis of the larger 5.89 GeV data set, during which time trigger thresholds were lower and correspondingly background rates were higher. Initial calibrations and data quality checks have just been completed on the 5.89 GeV data set, with asymmetry and background studies to follow shortly.

The extraction of the neutron asymmetry A_1^n at 4.73 GeV beam energy is also underway, however, the extraction is model-dependent. Previous experiments [17] have used Bissey *et al.*'s complete model in the DIS regime [26]. However, E06-014's 4.73 GeV data set spans both the DIS and resonance regions. A consistent treatment of both DIS and resonance data requires careful consideration of structure-function smearing [27]. We are working with W. Melnitchouk to extract neutron asymmetries across our entire kinematic range.
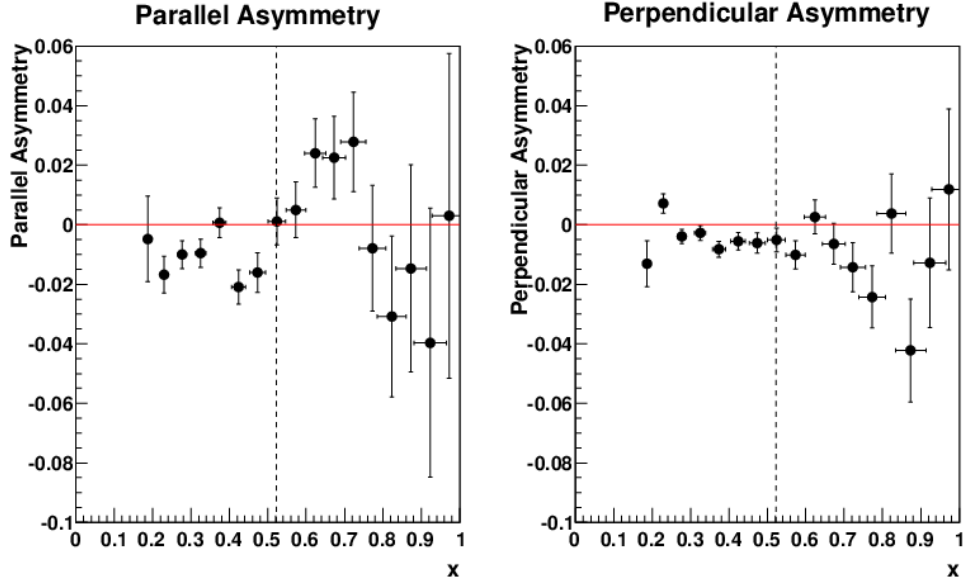
Figure 9: Preliminary $A_\parallel$ and $A_\perp$ on ^{3}He are plotted vs x at a beam energy of 4.73 GeV [2]. The dashed line is $W = 2$ GeV, which distinguishes the DIS region (to the left of the dashed line) from the resonance region (to the right of the dashed line).
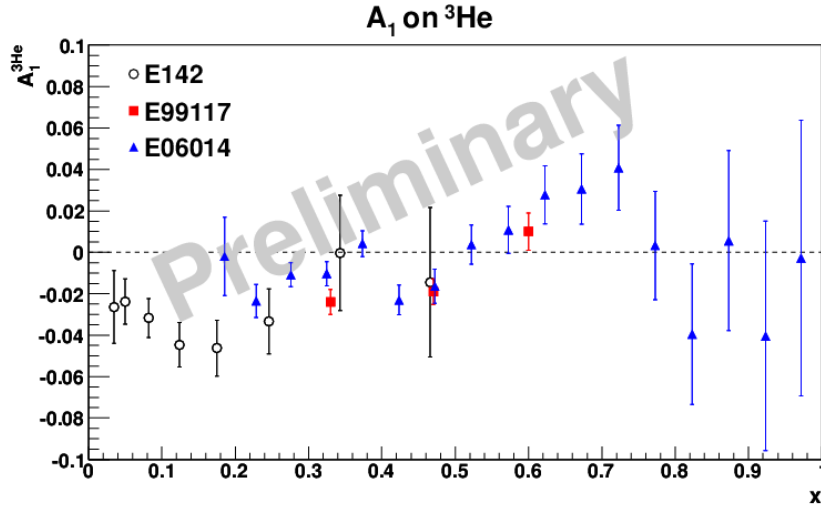

Figure 10: Preliminary E06-014 measurement of $A_1^{3\text{He}}$ at 4.73 GeV, compared to ^{3}He data from E142 at SLAC [28] and E99-117 in Hall A [17] [2].

References

[1] D. Parno *et al.*, http://hallaweb.jlab.org/experiment/E06-014/talks/index.html, E06014 Analysis Status Report (12/2010)

[2] D. Parno, PhD thesis, Carnegie Mellon University (2011).

[3] D. Parno *et al.*, Proceedings of the 2010 International Nuclear Physics Conference, J. Phys.: Conf. Ser. **312** 052018 (2011), arXiv:1106.4851 [physics.ins-det]

[4] M. Friend *et al.*, arXiv:1108.3116 [physics.ins-det]

[5] M. Burkardt, hep-ph/0905.4079v1 (2009).

[6] E. Stein *et al.*, Phys. Lett. B **343**, 369 (1995).

[7] M. Burkardt, AIP Conference Proceedings **1149**, 62 (2008), hep-ph/0902.0163v1.

[8] S. Choi, Z.-E. Meziani, X Jiang, B. Sawatzky, *et al.*, Jefferson Lab PAC PR-06-014 (2005).

[9] M. Gockeler *et al.*, Phys. Rev. D **72**, 054507 (2005), [arXiv:hep-lat/0506017].

[10] Shuyak and Vainshein, Nucl. Phys. B **201**, 141 (1982).

[11] Ji and Chou, Phys. Rev. D **42**, 3637 (1990).

[12] M. Amerian *et al.*, Phys. Rev. Lett. **89**, 242301 (2002); Phys. Rev. Lett. **92**, 022301 (2004); Phys. Rev. Lett. **93**, 152301 (2004); Z.-E. Meziani *et al.*, Phys. Lett. B **613**, 148 (2005); K. Slifer *et al.*, Phys. Rev. Lett. **101**, 22303 (2008).

[13] K. Slifer *et al.*, (Resonance Spin Structure) (2008), 0812.0031.

[14] D. Drechsel, S. S. Kamolov, and L. Tiatar, Eur. Phys. J. **A34**,69 (2007), 0710.0306.

[15] P. L. Anthony *et al.*, (E155), Phys. Lett. B **553**, 18 (2003), hep-ex/0204028.

[16] T. Averett, W. Korsch, Z.-E. Meziani, B. Sawatzky*et al.*, Jefferson Lab PAC E1206121 (2010).

[17] X. Zheng *et al.*, Phys. Rev. C **70**, 065207 (2004).

[18] K. V. Dharmawardane *et al.*, Phys. Lett. B **641**, 11 (2006).

[19] G. Cates, N. Liyanage, Z.-E. Meziani, G. Rosner, B. Wojtsekhowski, X. Zheng, *et al.*, Jefferson Lab PAC E1206122 (2006).

[20] G. Cates, J.-P. Chen, Z.-E. Meziani, X. Zheng *et al.*, Jefferson Lab PAC E1210101 (2010).

[21] I. Kominis, Ph.D. thesis, Princeton University (2001)

[22] Y. Zhang, Target analysis for E06-014. http://jlab.org/yawei/d2n/targ ana.html

[23] Y. Zhang, Electron paramagnetic resonance (EPR) project summary. Technical report, Hall A Collaboration (2011), http://www.jlab.org/yawei/weeklymeeting/110209/epr.pdf

[24] J. J. Lerose, Transfer Functions for Hall A Spectrometers, *http://hallaweb.jlab.org/news/minutes/tranferfuncs.html*

[25] V. Sulkosky, Ph.D. thesis, The College of William and Mary (2007).

[26] F. Bissey *et al.*, Phys. Rev. C **65**, 064317 (2002).

[27] S. A. Kulagin and W. Melnitchouk, Phys. Rev. C **78**, 065203 (2008).

[28] P. L. Anthony *et al.*, Phys. Rev. D **54**, 6620 (1996).